J. Fluid Mech. (1990), *vol.* 220, *pp.* 267–292
Printed in Great Britain

Dynamic compression and weak shock formation in an inert gas due to fast piston acceleration

By MENG WANG AND D. R. KASSOY
Department of Mechanical Engineering, University of Colorado, Boulder, CO 80309-0427, USA

(Received 14 March 1989 and in revised form 3 April 1990)

Unsteady gasdynamic concepts are used to model the piston-driven compression of a confined gas. Perturbation methods, based on the limit of small piston Mach number, are used to construct solutions. The piston Mach number increases smoothly from zero to a maximum value, $M_p = O(10^{-2})$ during an acoustic time period $t_a^* = O(10^{-4}\text{ s})$. A linear acoustic field is generated and is represented in terms of an infinite series of Fourier spatial modes. During the longer piston time period $t_p^* = O(10^{-2}\text{ s})$ the piston moves at constant speed. A multiple-timescale formulation is used to separate the instantaneous acoustic field from the accumulated bulk response of the gas to piston compression. The latter is found to be identical to the classical quasi-static results from equilibrium thermodynamic calculations. Nonlinear effects become important on the piston timescale. Modal interactions are represented by a system of coupled, nonlinear ordinary differential equations for the time-dependent Fourier coefficients. A numerical solution for this system describes the wavefront steepening to form a weak shock and its propagation back and forth repeatedly inside the cylinder.

1. Introduction

The piston-driven compression of a gas in an insulated cylinder is described frequently in terms of classical equilibrium thermodynamic concepts (Zemansky 1957). Isentropic relationships are employed to find the dependence of pressure and temperature on the instantaneous volume. At least formally, the piston speed must be vanishingly small in order to prevent the formation of spatial gradients of any type, to preclude the appearance of acoustic disturbances and to suppress significant fluid velocities which would have to be dissipated ultimately by viscous effects. These limitations would appear to prevent one from using classical arguments to describe processes in internal combustion engines, although there is an extensive literature on the subject (Obert 1970). In a typical engine with a shaft rotation rate of 3000 r.p.m. and a piston stroke of 0.08 m, one finds a maximum piston Mach number $M_p \approx 3.7 \times 10^{-2}$, a piston travelling time of approximately 10^{-2} s, and an acoustic wave travel time of about 2.4×10^{-4} s based on a sound speed of 340 m/s. The magnitudes of the timescales imply that it would be prudent to use a non-equilibrium formulation to describe this dynamic compression process.

Acoustic disturbances in a cylinder can be initiated and sustained by either mechanical energy input through a driving piston (Evans & Evans 1956; Chester 1964; Schneider 1981; Klein & Peters 1988), or by means of thermal energy supply at the boundary (Sirignano & Crocco 1964; Kassoy 1979; Radhwan & Kassoy 1984). The repeated reflections of the acoustic waves cause periodic oscillations of the velocity and thermodynamic properties of the gas. In the early study by Evans &

Evans (1956), the deviation of a piston-generated, shock-containing compression process from the isentropic process is estimated, based on the conservation equations for shocks (the Rankine–Hugoniot conditions). Their results are useful for evaluating irreversible effects caused by strong shock passage, but are not very relevant to studies of weak shocks that may actually appear in an engine cylinder, because the entropy change across the latter is known to be of third order in the shock strength (Landau & Lifshitz 1959). Later on Chester (1964) investigated theoretically the gasdynamic disturbances produced in a gas-filled tube by a vibrating piston using a small-Mach-number compressible flow model. His work is not engine-related either because the amplitude of the piston motion is very small relative to the length of the tube.

Schneider's (1981) study of the piston–cylinder problem is based on multiple reflections of a weak shock generated by an initial impulsive piston motion. The piston displacement is of the same order of magnitude as the length of the cylinder. Characteristic methods are used to solve the gasdynamic equations in order to follow the path of the shock. A multiple-timescale analysis is used to resolve the many shock reflections that occur during the relatively long period of piston motion. The results are used to explain how multiple passages of a weak shock through a cylinder causes the observed bulk compression process. More recently Klein & Peters (1988) have used a related approach to study weak pressure wave propagation and evolution processes in a piston–cylinder system, and their role on the development of a thermal explosion in a reactive gas. Their results show explicitly the shock formation process evolving from initially smooth compression waves, based on the development of multiple-valued regions in the characteristic space.

An impulsive piston motion in a finite cylinder will generate a shock wave instantaneously with an amplitude determined by the piston Mach number (Kevorkian & Cole 1981). In contrast, when a piston accelerates smoothly from rest linear acoustic waves are generated initially. The amplitude of the wave field depends upon the piston acceleration and its Mach number. Nonlinear accumulation effects will cause the acoustic wavefront to be transformed into a weak shock if the wave is strong enough, and if there are sufficient time to permit the nonlinearity to develop fully before the piston reaches the opposite cylinder endwall. It would, therefore, be very interesting to examine in a systematic way the entire process of wave generation, its later evolution and possible shock formation. In this paper we concentrate on the case of fast piston acceleration that occurs on the short acoustic timescale. Waves induced by much slower piston acceleration occurring on the piston timescale are considered in a separate paper (Wang & Kassoy 1990*a*).

In the present work the modelling of a piston-driven compression is based on the one-dimensional, unsteady equations for a perfect gas with transport effects. The gas is confined laterally between a fixed wall and a moving piston. The latter accelerates from rest to a Mach number $M = O(10^{-2})$ during an acoustic time period, $t_a^* = O(10^{-4}\ \mathrm{s})$, and then moves at constant speed for a considerably longer piston time period, $t_p^* = O(10^{-2}\ \mathrm{s})$. It is assumed in this model that the cylinder sidewalls do not have any effect on the planar gasdynamical process generated by the piston motion. The goal of the study is to predict the transient response of the gas to the piston motion prior to the time at which the piston reaches the fixed cylinder endwall.

An appropriate non-dimensionalization of the complete equations is used to demonstrate that transport effects are limited to thin thermal accommodation layers adjacent to the solid surfaces, of the type examined by Rott (1980). Isentropic nonlinear gasdynamic equations describe the fundamental physics everywhere else.

The generation of a linear acoustic field by continuous piston acceleration on the acoustic timescale is described first. The solution is expressed in terms of an infinite series of Fourier spatial modes. This linear acoustic solution is valid until $t^* \sim O(t_a^* t_p^*)^{\frac{1}{2}} = O(10^{-3}\text{ s})$, when the frequency of the wavefront reflections is altered in an important way by compression of the cylinder gas. A multiple-timescale analysis capable of resolving the frequency variations is applied to extend the linear acoustic solution to a longer timescale.

On the piston-passage timescale the acoustic waves continue to propagate in the compressing gas. A multiple-timescale analysis is again employed to separate the bulk compression from the acoustic phenomena. The development of nonlinear phenomena causes mode coupling in the Fourier series analysis, so that the time-dependent Fourier coefficients are described by an infinite system of nonlinear, ordinary differential equations. Numerical evaluation of the coefficients is obtained from a suitably truncated version of the system. The results obtained from series summation show the steepening of the compression wavefront and the formation of a weak shock. They also provide an explicit representation of the accumulated bulk compression arising from the passage of travelling waves which are reflected repeatedly at the boundaries. The former is simply that obtained from classical thermodynamic arguments. As the piston moves towards the cylinder endwall the wave passage frequency increases, as a result of increased sound speed and reduced wave travelling distance. A uniformly valid, composite solution, covering the entire time period, is constructed.

2. Mathematical formulation

The dynamic compression process is examined in the one-dimensional model of a piston–cylinder configuration shown in figure 1. Initially the gas is at rest and in an equilibrium state (p_0^*, ρ_0^*, T_0^*) inside a cylinder of length L^*. The acoustic timescale is defined by $t_a^* = L^*/c_0^*$, where the undisturbed speed of sound is $c_0^* = (\gamma R^* T_0^*)^{\frac{1}{2}}$. In contrast, the much longer conduction timescale is defined by $t_c^* = L^{*2}/\kappa_0^*$, where κ_0^* is the thermal diffusivity of the initial state.

The complete non-dimensional equations describing the physical system in figure 1 can be written in the form (Kassoy 1979)

$$p = \rho T, \tag{1}$$

$$\rho_t + (\rho u)_x = 0, \tag{2}$$

$$\rho(u_t + u u_x) = -\frac{p_x}{\gamma} + \delta \tfrac{4}{3}(\mu u_x)_x, \tag{3}$$

$$\rho C_v(T_t + u T_x) = -(\gamma - 1) p u_x + \delta\left[\frac{\gamma}{Pr}(k T_x)_x + \tfrac{4}{3}\gamma(\gamma-1)\mu u_x^2\right], \tag{4}$$

where the subscripts t and x denote partial derivatives. The non-dimensional variables are defined in terms of dimensional quantities (with asterisk) by

$$\left.\begin{aligned} \rho &= \frac{\rho^*}{\rho_0^*}, \quad p = \frac{p^*}{p_0^*}, \quad T = \frac{T^*}{T_0^*}, \quad u = \frac{u^*}{c_0^*}, \quad t = \frac{t^*}{t_a^*}, \\ x &= \frac{x^*}{L^*}, \quad \mu = \frac{\mu^*}{\mu_0^*}, \quad k = \frac{k^*}{k_0^*}, \quad C_v = \frac{C_v^*}{C_{v0}^*}, \end{aligned}\right\} \tag{5}$$

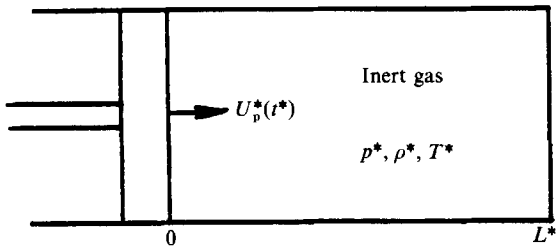

FIGURE 1. The physical system: an ideal inert gas undergoing piston-driven compression in a cylinder.

where μ^*, k^*, and C_v^* represent the dynamic viscosity, thermal conductivity and specific heat at constant volume, respectively. The parameter γ is the ratio of specific heats and

$$\delta = \frac{t_a^*}{t_c^*} Pr, \quad Pr = \frac{C_{p0}^* \mu_0^*}{k_0^*}, \tag{6}$$

where the former is basically a Knudsen number. For air at standard conditions ($p_0^* = 1$ atm, $T_0^* = 300$ K) and $L^* = 0.08$ m, the typical Prandtl number $Pr = O(1)$, and then $\delta = O(10^{-6})$. The specific heats are assumed constant so that $C_v = 1$. Calculations using isentropic relations based on the properties of air (Bolz & Tuve 1973) show that, even for a compression ratio as high as 10, the error arising from the constant C_v^* approximation is less than 5%.

The initial conditions are simply

$$t = 0; \quad p = \rho = T = 1, \quad u = 0. \tag{7}$$

On the solid surfaces the dynamic boundary conditions can be written as

$$x = X_p(t); \quad u \equiv U_p(t) = \epsilon f'(t), \tag{8}$$

$$x = 1; \quad u = 0, \tag{9}$$

where $X_p(t)$ is the piston location and $U_p(t)$ the piston speed. The parameter ϵ is the maximum piston Mach number defined as the ratio of the maximum piston speed to the speed of the sound c_0^*,

$$\epsilon = \frac{U_{p\max}^*}{c_0^*}. \tag{10}$$

Typically $\epsilon = O(0.05)$. The function $f'(t)$ is an order-one quantity (the prime denotes a derivative) which describes the piston motion with time. A piston velocity variation typical of those to be considered is shown in figure 2.

Solutions to the basic system (1)–(4) and (7)–(9) are to be sought in the limit $\epsilon \to 0, \delta \to 0$ where it is noted that $\delta \ll \epsilon$. The limiting forms of (3) and (4) imply that transport effects may be important in very thin accommodation layers, adjacent to solid surfaces, of the type considered by Rott (1980). In addition, sufficiently high-frequency, short-wavelength acoustic phenomena will be viscous and heat conducting. Nonetheless, the most important physical processes in the cylinder can be described by the inviscid, non-conducting versions of (3) and (4). The dissipation effects are in general too weak to cause acoustic damping on the timescale considered. In this respect, the state, continuity and energy equations can be combined to give the familiar results

$$p = \rho^\gamma + O(\delta), \quad T = \rho^{\gamma-1} + O(\delta). \tag{11}$$

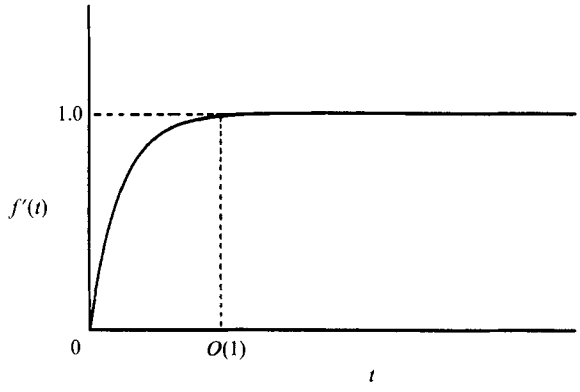

FIGURE 2. Piston velocity function.

It follows from (3) that the momentum equation can be written as

$$\rho(u_t+uu_x) = -\rho^{\gamma-1}\rho_x+O(\delta). \tag{12}$$

It should be pointed out that if shock waves are present in the system, transport effects play a vital role in the extremely thin layer where velocity and thermodynamic properties of the gas experience a sudden change. However, from a practical point of view the gas properties on both sides of the shock and their increments across the shock are of major interest, rather than the internal structure of the shock wave. A weak solution of the Euler equations (2) and (12) alone can correctly provide these values.

It is also to be emphasized that the one-dimensional unsteady model employed in this study is used to determine the explicit effects of gasdynamical processes on equilibrium compression. In this sense we do not address the effects of non-planar flow (e.g. vortices and turbulence) or of thermal conduction on the cylinder sidewalls. Given the timescale of the piston stroke, perhaps a few thousandths of a second, it is not likely that heat exchange with sidewalls will have a noticeable effect on the process described below.

The analysis is carried out most efficiently in terms of the Lagrangian variable

$$s = \int_{X_p(t)}^{x} \rho(\hat{x}, t)\,\mathrm{d}\hat{x}, \tag{13}$$

because the fluid mass in the cylinder is constant. The piston surface $x = X_p(t)$ is represented by $s = 0$, while the fixed endwall corresponds to $s = 1$ as a result of mass conservation. Equation (13) can be used in (2) and (12) to find

$$\rho_t+\rho^2u_s = 0, \quad u_t+\rho^{\gamma-1}\rho_s = O(\delta). \tag{14}$$

The appropriate initial conditions are given in (7), while the boundary conditions take the form

$$s = 0; \quad u = \epsilon f'(t), \qquad s = 1; \quad u = 0. \tag{15}$$

Once ρ and u are obtained, the pressure and temperature are found from the results in (11). The mathematical methods employed here are derived from related studies of thermal–mechanical processes by Kassoy (1979), Poland & Kassoy (1983), Radhwan & Kassoy (1984) and from multiple-timescale oscillatory dynamical systems discussed by Kevorkian & Cole (1981).

3. Linear acoustic theory

The piston speed $U_p = O(\epsilon)$ induces both mechanical and thermodynamical disturbances of similar magnitude into the gas. As a result, the scaling transformations

$$u = \epsilon\bar{u}(t, s; \epsilon), \quad \rho = 1 + \epsilon\bar{\rho}(t, s; \epsilon) \tag{16}$$

can be used in (14), (15) and (7) to derive the lowest-order approximate system valid in the limit $\epsilon \to 0$,

$$\bar{\rho}_t + \bar{u}_s = 0, \quad \bar{u}_t + \bar{\rho}_s = 0. \tag{17}$$

$$t = 0; \quad \bar{u} = \bar{\rho} = 0. \tag{18}$$

$$s = 0; \quad \bar{u} = f', \qquad s = 1; \quad \bar{u} = 0. \tag{19}$$

It follows that the velocity field is described by

$$\bar{u}_{tt} - \bar{u}_{ss} = 0, \tag{20}$$

$$t = 0; \quad \bar{u} = \bar{u}_t = 0, \tag{21}$$

along with the boundary conditions (19). Either Laplace transform methods (Kassoy 1979; Radhwan & Kassoy 1984) or a technique described by Courant & Hilbert (1953) can be used to obtain solutions.

The short-time result

$$\bar{u} = \begin{cases} f'(t-s), & s < t \leqslant 1, \\ 0, & t < s \leqslant 1, \end{cases} \tag{22}$$

describes the velocity field between the piston and the fixed endwall prior to the time at which the wavefront reaches the latter. Equations (17) then give an identical solution for $\bar{\rho}$. At $s = t$ there is a jump in the gradient of $f'(t)$ rather than the function itself. Thus $s = t$ is a surface of weak discontinuity representing the acoustic wavefront. Further developments, including explicit individual wavefront reflections can be followed using a format described by Miles (1971). However, it is equally informative to write the general solution as

$$\bar{u} = f'(t)(1-s) + \sum_{n=1}^{\infty} A_n(t) \sin(n\pi s), \tag{23}$$

$$A_n(t) = -\frac{2}{n\pi} \int_0^t f''(\hat{t}) \cos[n\pi(\hat{t}-t)]\, \mathrm{d}\hat{t}. \tag{24}$$

An integration of (17) for $\bar{\rho}_t$ and $\bar{\rho}_s$ gives the density perturbation,

$$\bar{\rho} = f(t) - \sum_{n=1}^{\infty} I_n(t) \cos(n\pi s), \tag{25}$$

where

$$I_n(t) = \frac{2}{n\pi} \int_0^t f''(\hat{t}) \sin[n\pi(\hat{t}-t)]\, \mathrm{d}\hat{t} \tag{26}$$

and $f(0) = 0$. In general, the piston motion depicted in figure 2 has the asymptotic property $f(t \to \infty) \sim t + O(1)$, so that $A_n(t \to \infty) = O(1)$ and $I_n(t \to \infty) = O(1)$.

The results in (23) and (25) demonstrate in an explicit manner that the gas response can be described in terms of two distinct effects. In each equation the first

term describes the bulk response of the gas at time t, which is the accumulated effect of multiple passages of compressive acoustic waves across the cylinder. The density variation, $f(t)$, corresponds to the result found from a traditional thermodynamic analysis of compression. The second term is a Fourier representation of the instantaneous acoustic field.

In the limit $t \to \infty$, solutions (23) and (25) take the form

$$u(t \to \infty, s) \sim \epsilon \left[(1-s) + \sum_{n=1}^{\infty} A_n(t \to \infty) \sin(n\pi s) \right] + \ldots, \tag{27}$$

$$\rho(t \to \infty, s) \sim 1 + \epsilon \left[t - \sum_{n=1}^{\infty} I_n(t \to \infty) \cos(n\pi s) \right] + \ldots. \tag{28}$$

Equation (28) indicates that a non-uniformity occurs when $t = O(\epsilon^{-1})$ as a result of bulk compression. This is, however, not the earliest singularity in the asymptotic expansions. Let $\bar{u} = \bar{u}_1 + \epsilon \bar{u}_2 + \ldots, \bar{\rho} = \bar{\rho}_1 + \epsilon \bar{\rho}_2 + \ldots$ and derive the higher-order approximation to (14). The system for $\bar{u}_2$ is given by

$$\left.\begin{aligned} \bar{u}_{2tt} - \bar{u}_{2ss} &= -\tfrac{1}{2}(\gamma+1)(\bar{\rho}_1^2)_{st}, \\ t = 0; \quad \bar{u}_2 &= \bar{u}_{2t} = 0, \\ s = 0, 1; \quad \bar{u}_2 &= 0, \end{aligned}\right\} \tag{29}$$

where $\bar{\rho}_1$ is given in (25), (26). The non-homogeneous forcing function in (29) is the source of a secular term in the $\bar{u}_2$-solution which is $O(t^2)$ for $t \to \infty$, for the type of piston motion depicted in figure 2. For example, if the piston motion is specified by the function $f(t) = t + e^{-t} - 1$, the asymptotic behaviour of $\bar{u}_2$ as $t \to \infty$ is found from (29):

$$\lim_{t \to \infty} \bar{u}_2 = \tfrac{1}{2}(\gamma+1) t^2 \sum_{n=1}^{\infty} \frac{\sin(n\pi s)}{1 + n^2\pi^2} [\sin(n\pi t) - n\pi \cos(n\pi t)] + O(t). \tag{30}$$

If the total velocity is written as $u = \epsilon \bar{u}_1 + \epsilon^2 \bar{u}_2 + \ldots$, it is found that the non-uniformity occurs first in the velocity solution at $t = O(\epsilon^{-\frac{1}{2}})$, when the basic density variation is like $\rho \sim 1 + O(\epsilon^{\frac{1}{2}})$ from (28). The breakdown of u at $t = O(\epsilon^{-\frac{1}{2}})$ implies that $\epsilon^{\frac{1}{2}} t$ is an important new timescale. It actually represents the time at which the compression of the gas becomes sufficiently large to alter substantially the frequency of the acoustic wave passages across the cylinder. As will be shown, this is the cause of the $O(t^2)$ secular growth exhibited in the velocity solution $\bar{u}_2$.

4. Extended acoustic theory

The non-uniformity in the asymptotic solutions which occurs at $t = O(\epsilon^{-\frac{1}{2}})$ can be eliminated by using a multiple-timescale analysis. A new time variable is defined by

$$\sigma = \epsilon^{\frac{1}{2}} t \tag{31}$$

and σ is treated as though it were independent of t (Kevorkian & Cole 1981), although the relation (31) holds. As a result, the ordinary time derivative in (14) must be replaced by

$$\left(\frac{\partial}{\partial t}\right)_s = \left(\frac{\partial}{\partial t}\right)_{\sigma, s} + \epsilon^{\frac{1}{2}} \left(\frac{\partial}{\partial \sigma}\right)_{t, s}. \tag{32}$$

The subscripts refer to independent variables held constant in each of the derivatives. Equations (14) and their initial conditions (7) become

$$\rho_t + \epsilon^{\frac{1}{2}}\rho_\sigma + \rho^2 u_s = 0, \tag{33}$$

$$u_t + \epsilon^{\frac{1}{2}}u_\sigma + \rho^{\gamma-1}\rho_s = 0, \tag{34}$$

and

$$t = \sigma = 0; \quad \rho = 1, \quad u = u_t + \epsilon^{\frac{1}{2}}u_\sigma = 0. \tag{35}$$

The boundary conditions are given in (15). For the limit $\epsilon \to 0$ the velocity and density are expressed as

$$u = \epsilon u_1 + \epsilon^{\frac{3}{2}}u_2 + \ldots, \tag{36}$$

$$\rho = 1 + \epsilon^{\frac{1}{2}}\rho_0 + \epsilon\rho_1 + \epsilon^{\frac{3}{2}}\rho_2 + \ldots. \tag{37}$$

When (36) and (37) are used in (33)–(35), the lowest-order equations imply that

$$\rho_0 = \rho_0(\sigma), \quad \rho_0(\sigma = 0) = 0, \tag{38}$$

which indicates that ρ_0 is a function of the longer timescale only.

The next-order approximate equations are

$$\rho_{1t} + u_{1s} = -\rho_0'(\sigma), \quad u_{1t} + \rho_{1s} = 0, \tag{39}$$

which can be combined to give

$$u_{1tt} - u_{1ss} = 0. \tag{40}$$

Initial and boundary conditions are derived from (15) and (35):

$$t = \sigma = 0; \quad u_1 = u_{1t} = 0, \tag{41}$$

$$s = 0; \quad u_1 = f'(t), \qquad s = 1; \quad u_1 = 0. \tag{42}$$

The general solution to (40)–(42) is written as

$$u_1 = f'(t)(1-s) + \sum_{n=1}^{\infty} B_n(t, \sigma)\sin(n\pi s), \tag{43}$$

where

$$B_n(t, \sigma) = C_n(\sigma)\cos(n\pi t) + D_n(\sigma)\sin(n\pi t) + \frac{2}{n^2\pi^2}\int_0^t \sin[n\pi(\hat{t}-t)]f'''(\hat{t})\,\mathrm{d}\hat{t}. \tag{44}$$

The functions $C_n(\sigma)$ and $D_n(\sigma)$ are to be determined from the next-higher-order approximate equations. Their initial values are obtained by substituting (43), (44) into (41):

$$C_n(0) = -\frac{2}{n\pi}f'(0), \quad D_n(0) = -\frac{2}{n^2\pi^2}f''(0). \tag{45}$$

In the derivation of (45), the first term in (43) has to be Fourier decomposed with respect to s and expressed in terms of Fourier sine series.

The slowly varying function $\rho_0(\sigma)$ can be determined uniquely at this stage. If (39) and (43) are combined one obtains

$$\rho_{1t} = -\rho_0'(\sigma) + f'(t) - \sum_{n=1}^{\infty} n\pi B_n(t, \sigma)\cos(n\pi s). \tag{46}$$

If $B_n(t, \sigma)$ is assumed to be well-behaved (harmonic or exponential decay with time) as $t \to \infty$, then to suppress $O(t)$ growth in ρ_1 the following relation must be enforced:

$$\lim_{t\to\infty}[-\rho_0'(\sigma) + f'(t)] = 0. \tag{47}$$

Given the $f'(t)$-behaviour in figure 2, this gives

$$\rho_0 = \sigma, \tag{48}$$

which satisfy conditions given in (38).

The higher-order analogue to (40) can be obtained from (33)–(37), and by suitable recombination one finds

$$u_{2tt} - u_{2ss} = -2u_{1\sigma t} + (\gamma+1)\rho_0 u_{1ss}. \tag{49}$$

Equations (43), (44) and (48) can be used in (49) to show that

$$u_{2tt} - u_{2ss} = -\sum_{n=1}^{\infty} F_n(t,\sigma)\sin(n\pi s), \tag{50}$$

where

$$\begin{aligned} F_n(t,\sigma) = {} & [2n\pi D_n'(\sigma) + (\gamma+1)\, n^2\pi^2\sigma C_n(\sigma)]\cos(n\pi t) \\ & + [-2n\pi C_n'(\sigma) + (\gamma+1)\, n^2\pi^2\sigma D_n(\sigma)]\sin(n\pi t) \\ & + 2(\gamma+1)\,\sigma\int_0^t \sin[n\pi(\hat{t}-t)] f'''(\hat{t})\,\mathrm{d}\hat{t}. \end{aligned} \tag{51}$$

Thus far, the piston motion function $f(t)$ is arbitrary as long as it satisfies the properties described in figure 2. For a specified $f(t)$ the integral in (51) can be evaluated. One identifies that terms proportional to $\cos(n\pi t)$ and $\sin(n\pi t)$ in F_n are resonant forcing terms because, when used in (50), they generate $O(t)$ growth in the particular solution of u_2. These terms must be eliminated by setting their coefficients equal to zero. As an example calculation, we adopt the function mentioned previously, i.e.

$$f(t) = t + \mathrm{e}^{-t} - 1, \tag{52}$$

to describe the piston motion. Using (52) in (51) and eliminating all the resonant terms leads to

$$\left.\begin{aligned} D_n'(\sigma) + \tfrac{1}{2}(\gamma+1)\, n\pi\sigma C_n(\sigma) - \frac{\gamma+1}{1+n^2\pi^2}\sigma = 0, \\ C_n'(\sigma) - \tfrac{1}{2}(\gamma+1)\, n\pi\sigma D_n(\sigma) - \frac{\gamma+1}{n\pi(1+n^2\pi^2)}\sigma = 0. \end{aligned}\right\} \tag{53}$$

Equations (53) are solved analytically subject to the initial conditions in (45). The results, together with (52), can be inserted into (44). After some rearrangements it follows that

$$B_n(t,\sigma) = \frac{2}{n\pi}\left\{\frac{\mathrm{e}^{-t}}{1+n^2\pi^2} - \frac{1}{(1+n^2\pi^2)^{\frac{1}{2}}}\sin[n\pi(t+\tfrac{1}{4}(\gamma+1)\,\sigma^2+\phi_n)]\right\}, \tag{54}$$

where

$$\phi_n = \frac{1}{n\pi}\tan^{-1}\left(\frac{1}{n\pi}\right). \tag{55}$$

Obviously B_n in (54) has the well-behaved character assumed earlier. The velocity is thus obtained from (43). To complete the density solution, the two first-order differential equations for ρ_1 in (39) are integrated to provide the result

$$\rho_1 = 2\sum_{n=1}^{\infty}\left\{\frac{\mathrm{e}^{-t}}{1+n^2\pi^2} - \frac{1}{n\pi(1+n^2\pi^2)^{\frac{1}{2}}}\cos[n\pi(t+\tfrac{1}{4}(\gamma+1)\,\sigma^2+\phi_n)]\right\}\cos(n\pi s) + \mathrm{e}^{-t} + h(\sigma), \tag{56}$$

where $h(\sigma)$ is an integration constant, to be found from higher-order considerations.

Equations (51)–(53) can be used in (50) to obtain the following differential equation for u_2:

$$u_{2tt} - u_{2ss} = -2(\gamma+1)\,\sigma\,\mathrm{e}^{-t} \sum_{n=1}^{\infty} \frac{n\pi}{1+n^2\pi^2} \sin(n\pi s). \tag{57}$$

The corresponding initial and boundary conditions are derived from (15) and (35)–(37):

$$t = \sigma = 0; \quad u_2 = 0, \quad u_{2t} + u_{1\sigma} = 0, \tag{58}$$

$$s = 0; \quad u_2 = 0, \qquad s = 1; \quad u_2 = 0. \tag{59}$$

The solution to (57)–(59) is written in the form

$$u_2 = \sum_{n=1}^{\infty} \left[a_n(\sigma)\cos(n\pi t) + b_n(\sigma)\sin(n\pi t) - 2(\gamma+1)\frac{n\pi}{(1+n^2\pi^2)^2}\,\sigma\,\mathrm{e}^{-t} \right] \sin(n\pi s), \tag{60}$$

with

$$a_n(0) = b_n(0) = 0, \tag{61}$$

where $a_n(\sigma)$ and $b_n(\sigma)$ can be determined only from higher-order considerations. Fortunately their exact forms are not needed to find the function $h(\sigma)$ in (56). As a result one can consider the equation for ρ_2 derived from (33), (36) and (37):

$$\rho_{2t} = -\rho_{1\sigma} - 2\rho_0 u_{1s} - u_{2s}. \tag{62}$$

When the expressions for ρ_0, ρ_1, u_1 and u_2 are used in (62), and the resulting terms are rearranged, it is found that the term $-h'(\sigma)+2\sigma$ will lead to secular growth in ρ_2 upon integration. Therefore it is required that

$$-h'(\sigma) + 2\sigma = 0. \tag{63}$$

The solution of (63) under the initial condition $\rho_1(t = \sigma = 0) = 0$ is then

$$h(\sigma) = \sigma^2 - 1. \tag{64}$$

The results developed in this section can be combined to express the velocity and density solutions accurate to $O(\epsilon)$ that describe the compression process during the extended acoustic time period:

$$u = \epsilon \left\{ (1-\mathrm{e}^{-t})(1-s) + \sum_{n=1}^{\infty} \frac{2}{n\pi} \left[\frac{\mathrm{e}^{-t}}{1+n^2\pi^2} - \frac{1}{(1+n^2\pi^2)^{\frac{1}{2}}} \sin\left(n\pi\left(t + \tfrac{1}{4}(\gamma+1)\,\sigma^2 + \phi_n\right)\right) \right] \sin(n\pi s) \right\} + O(\epsilon^{\frac{3}{2}}), \tag{65}$$

$$\rho = 1 + \epsilon^{\frac{1}{2}}\sigma + \epsilon \left\{ \mathrm{e}^{-t} - 1 + \sigma^2 + 2 \sum_{n=1}^{\infty} \left[\frac{\mathrm{e}^{-t}}{1+n^2\pi^2} - \frac{1}{n\pi(1+n^2\pi^2)^{\frac{1}{2}}} \cos\left(n\pi\left(t + \tfrac{1}{4}(\gamma+1)\,\sigma^2 + \phi_n\right)\right) \right] \cos(n\pi s) \right\} + O(\epsilon^{\frac{3}{2}}). \tag{66}$$

In (65) and (66), terms inside the summation signs are Fourier decompositions of the evolving acoustic disturbances in the Lagrangian coordinate system. The accumulated effect of acoustic wave transmission up to time (t, σ) is the spatially

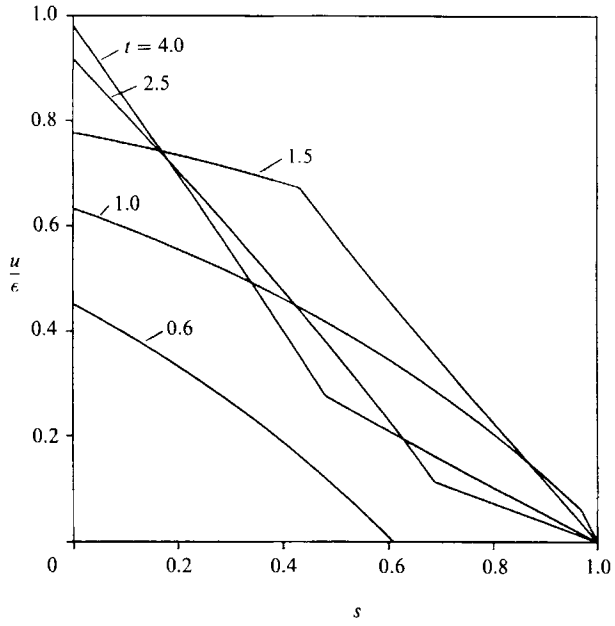

FIGURE 3. The velocity distribution in terms of Lagrangian variable s during the piston acceleration period as obtained from (65). The maximum piston Mach number $\epsilon = 0.05$, and $\gamma = 1.4$.

homogeneous bulk fluid response, which is represented by terms outside the summations. Except for the transient terms, proportional to e^{-t}, inside the square brackets, which affect only a very short initial period, the amplitude of each Fourier mode is basically periodic in time with slowly growing frequency according to $1+[\frac{1}{4}(\gamma+1)]\epsilon t$. This frequency variation was not included in the single-timescale solutions (23)–(26) and hence the $O(t^2)$ secular growth in the higher-order velocity expansion resulted. The maximum amplitudes of the Fourier modes are independent of time and decay rapidly as the mode number n increases. In the limit $\sigma \to 0$, which corresponds to very small piston displacement and weak compression of the gas, the equivalence of (65), (66) to (23)–(26) can be easily checked if the piston motion function (52) is applied to (23)–(26).

Figure 3 displays the generation and development of the velocity disturbance in the confined gas during the acceleration period of the piston, which is of the same order of magnitude as the acoustic timescale. The vertical axis represents the gas velocity magnified by a factor ϵ^{-1}, and the horizontal axis is the Lagrangian coordinate. The velocity distribution in this Lagrangian system is calculated from (65) by summing 200 Fourier terms, and plotted for a succession of acoustic times indicated above each curve, when the piston Mach number $\epsilon = 0.05$. Calculations based on summations of more Fourier modes were also conducted, and the results exhibited no appreciable change in the velocity curves.

Once the piston is accelerated smoothly from rest, it creates acoustic signals which propagate in the gas medium with the local speed of sound. As the acoustic wavefront propagates, it imparts a finite-velocity disturbance along its passage in the initially quiescent system. At $t = 0.6$ the acoustic wavefront has not yet reached the opposite cylinder endwall at $s = 1$ and the region ahead of the wavefront remains undisturbed. By the time $t = 1$ the wavefront reaches the cylinder wall. It is then reflected and its direction of propagation is reversed. The compression wave

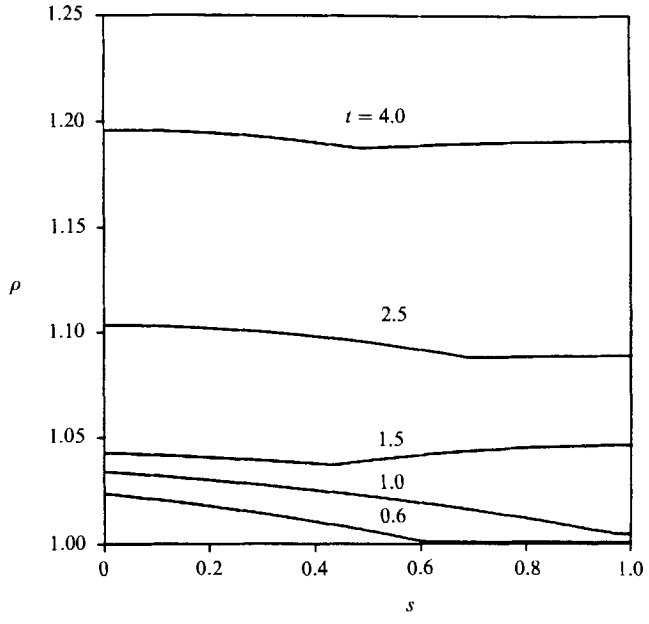

FIGURE 4. The density distribution in terms of the Lagrangian variable s during the piston acceleration period as obtained from (66). The maximum piston Mach number $\epsilon = 0.05$, and $\gamma = 1.4$.

decelerates the gas it encounters. Meanwhile the velocity of the gas ahead of the now backward-travelling wavefront continues to increase as a result of additional acoustic signals being emitted from the accelerating piston surface. In this way the acoustic signals continue to be reflected back and forth across the cylinder, generating the bulk compression effect. The velocity profiles in figure 3 are always continuous. Discontinuities occur only in the first derivative of velocity at the acoustic wavefronts. In figure 4 the corresponding density distribution inside the cylinder is plotted for the same set of time values. One may observe clearly the steady buildup of gas density with time as the compression wavefront travels back and forth between the two confining walls. The pressure and temperature spatial distributions have similar characteristics, given the isentropic relations in (11).

In summary, we have successfully extended the time range of uniformly valid acoustic time solutions for both u and ρ to $t = O(\epsilon^{-\frac{1}{2}})$ or $\sigma = O(1)$, where σ is a timescale intermediate in the logarithmic sense between the short acoustic time and the long piston time. On timescale σ the compression effect becomes significant enough to shift the frequency of acoustic wave reflections in the cylinder. By taking into account this frequency change, the $O(t^2)$ mixed secular growth found in the velocity expansion in §3 is eliminated. It should be emphasized, though, that no appreciable waveform deformation related with nonlinear phenomena is observed on the timescale σ. Mathematically the solutions developed in this section still belong to the linear regime due to the linear nature of the secular equations (53), which determine the Fourier coefficients and hence the acoustic wave shape. The nonlinear accumulation effects are expected to become pronounced on the still longer piston time $t \sim O(\epsilon^{-1})$, which is the subject of the next section.

5. Compression on the piston timescale

The solution described in (66) is not uniformly valid when $\sigma \sim \epsilon^{-\frac{1}{2}}$ or $t \sim \epsilon^{-1}$, showing that when the piston has travelled an $O(1)$ distance from its initial location, the extended acoustic timescale σ is no longer appropriate. Instead, one must define another important timescale

$$\tau = \epsilon t = \frac{t^*}{t_{\mathrm{p}}^*}, \quad t_{\mathrm{p}}^* = \frac{L^*}{U_{\mathrm{pmax}}^*}, \tag{67}$$

which can be used to study more extensive gas compression. Here t_{p}^* is the characteristic piston passage time.

Given the form in (65) and (66), the velocity and density are expressed as

$$u = \epsilon \tilde{u}(t, \tau, s; \epsilon), \quad \rho = \rho_0(\tau) + \epsilon \tilde{\rho}(t, \tau, s; \epsilon), \tag{68}$$

for the limit $\epsilon \to 0$, and a multiple-timescale formulation is again employed by using the relation

$$\left(\frac{\partial}{\partial t}\right)_s = \left(\frac{\partial}{\partial t}\right)_{\tau, s} + \epsilon \left(\frac{\partial}{\partial \tau}\right)_{t, s}. \tag{69}$$

The lowest-order linear wave equation is obtained for $\tilde{u}$ from (14), (68) and (69):

$$\tilde{u}_{tt} - \rho_0^{\gamma+1}(\tau)\, \tilde{u}_{ss} = 0. \tag{70}$$

In this Lagrangian system the τ-dependent coefficient $\rho_0^{\gamma+1}(\tau)$ is equivalent to the square of the instantaneous sound speed, which is slowly varying with time. The frequency of the acoustic wave passage will accordingly vary with τ. The instantaneous wave-passage frequency across the cylinder is proportional to the sound speed $\rho_0^{\frac{1}{2}(\gamma+1)}$, while the phase of the wave passage is proportional to the integral of $\rho_0^{\frac{1}{2}(\gamma+1)}$ with respect to t since ρ_0 is not a constant. Under such circumstances the straightforward two-variable procedure in terms of t and τ fails and a transformed fast time variable

$$\tilde{t} = \int_0^t \rho_0^{\frac{1}{2}(\gamma+1)}(\epsilon \hat{t})\, \mathrm{d}\hat{t} \tag{71}$$

must be applied. This choice of fast time variable is obtained by an analogy of the current problem with the classical problem of the motion of a pendulum under slow variations in its length (Kevorkian & Cole 1981).

If $\tilde{t}$ and τ are used as fast and slow time variables respectively, and s as the space variable, then the first three order approximations of (14) are

$$\rho_{0\tilde{t}} = 0, \tag{72}$$

$$\rho_0^{\frac{1}{2}(\gamma+1)} \rho_{1\tilde{t}} + \rho_0^2 u_{1s} = -\rho_{0\tau}, \tag{73}$$

$$\rho_0^{\frac{1}{2}(\gamma+1)} \rho_{2\tilde{t}} + \rho_0^2 u_{2s} = -\rho_{1\tau} - 2\rho_0 \rho_1 u_{1s}, \tag{74}$$

and

$$\rho_{0s} = 0, \tag{75}$$

$$\rho_0^{\frac{1}{2}(\gamma+1)} u_{1\tilde{t}} + \rho_0^{\gamma-1} \rho_{1s} = 0, \tag{76}$$

$$\rho_0^{\frac{1}{2}(\gamma+1)} u_{2\tilde{t}} + \rho_0^{\gamma-1} \rho_{2s} = -u_{1\tau} - (\gamma-1)\, \rho_0^{\gamma-2} \rho_1 \rho_{1s}, \tag{77}$$

respectively, where the dependent variables in (72)–(77) are defined by

$$\rho = \rho_0 + \epsilon \rho_1 + \epsilon^2 \rho_2 + \ldots, \quad u = \epsilon u_1 + \epsilon^2 u_2 + \ldots. \tag{78}$$

Equations (72) and (75) indicate that $\rho_0 = \rho_0(\tau)$. A combination of (73) and (76) gives

$$u_{1\tilde{t}\tilde{t}} - u_{1ss} = 0, \tag{79}$$

which must satisfy boundary conditions derived from (15) and (78):

$$s = 0; \quad u_1 = 1, \qquad s = 1; \quad u_1 = 0. \tag{80}$$

The general solution to (79), (80) can be written as

$$u_1 = 1 - s + \sum_{n=1}^{\infty} [\alpha_n(\tau)\cos(n\pi\tilde{t}) + \beta_n(\tau)\sin(n\pi\tilde{t})]\sin(n\pi s). \tag{81}$$

Initial conditions, obtained by matching the piston time solution with the acoustic time solution, can be constructed from the asymptotic behaviour of (65) and (66) for $t \to \infty, \sigma \to \infty$:

$$u(\tilde{t}, \tau \to 0, s) \sim \epsilon\left\{1 - s + \ldots - \sum_{n=1}^{\infty} \frac{2}{n\pi(1+n^2\pi^2)^{\frac{1}{2}}} \times \sin[n\pi(t + \epsilon^{\frac{1}{4}}(\gamma+1)\,t^2 + \ldots + \phi_n)]\sin(n\pi s)\right\} + \ldots, \tag{82}$$

$$\rho(\tilde{t}, \tau \to 0, s) \sim 1 + \tau + \tau^2 + \ldots + \epsilon\left\{-1 - \sum_{n=1}^{\infty} \frac{2}{n\pi(1+n^2\pi^2)^{\frac{1}{2}}} \times \cos[n\pi(t + \epsilon^{\frac{1}{4}}(\gamma+1)\,t^2 + \ldots + \phi_n)]\cos(n\pi s)\right\} + \ldots. \tag{83}$$

A comparison of (82) with (81) implies that

$$\alpha_n(0) = -\frac{2}{n\pi(1+n^2\pi^2)}, \quad \beta_n(0) = -\frac{2}{1+n^2\pi^2}, \quad n = 1, 2, \ldots, \tag{84}$$

and

$$\tilde{t} \sim t + \epsilon^{\frac{1}{4}}(\gamma+1)\,t^2 + \ldots \quad \text{as} \quad \tau \to 0. \tag{85}$$

The two first-order differential equations for ρ_1 in (73) and (76) are integrated to give

$$\rho_1 = \rho_0^{\frac{1}{2}(3-\gamma)}\left\{\beta_0(\tau) + \sum_{n=1}^{\infty}[-\alpha_n(\tau)\sin(n\pi\tilde{t}) + \beta_n(\tau)\cos(n\pi\tilde{t})]\cos(n\pi s)\right\} + [\rho_0^2(\tau) - \rho_0'(\tau)]\,\tilde{t}\rho_0^{-\frac{1}{2}(\gamma+1)}, \tag{86}$$

where $\beta_0(\tau)$ is an integration constant representing the spatially homogeneous, slowly varying part in the Fourier series expression of ρ_1. Its explicit form is to be found from higher-order considerations, such that $\beta_0(\tau \to 0) = -1$.

In order to satisfy (83), and to prevent secular growth of ρ_1 relative to the variable $\tilde{t}$, the last term on the right-hand side of (86) must be suppressed. It follows that

$$\rho_0 = \frac{1}{1-\tau}. \tag{87}$$

Equation (87) describes the basic, spatially homogeneous density variation caused by decreasing cylinder volume associated with the piston motion. This zeroth-order solution is identical to the result obtained from a classical equilibrium thermodynamic calculation. The singularity at $\tau = 1$ occurs when the piston has reached the endwall at $X_p = 1$. In practical terms, the solution is valid only for $\tau < 1$.

The transformed fast time variable $\tilde{t}$ is calculated from (71) and (87),

$$\tilde{t} = \frac{1}{\epsilon}\frac{2}{\gamma-1}[(1-\tau)^{-\frac{1}{2}(\gamma-1)}-1]. \tag{88}$$

It satisfies (85) and is in agreement with acoustic time solutions in the limit $\tau \to 0$.

The unknown functions α_n, β_n and β_0 in (86) are determined by a procedure similar to that in §4, although the mathematical derivations in the present case are lengthier and more cumbersome. Interested readers should refer to Wang's (1989) dissertation for more details concerning the derivations of (89)–(96).

A suitable recombination of (74) and (77) gives

$$u_{2\tilde{t}\tilde{t}} - u_{2ss} = 2\rho_0^{-2}(\rho_{1\tau} + \tfrac{1}{4}(\gamma-7)\rho_0\rho_1)_s - \tfrac{1}{2}(\gamma+1)\rho_0^{\frac{1}{2}(\gamma-5)}(\rho_1^2)_{s\tilde{t}}. \tag{89}$$

The expressions for ρ_0 and ρ_1 are substituted into the forcing function on the right-hand side of (89), and the results are collected into different groups according to their resonant or non-resonant nature. Based on the same argument as lead to (53), resonant forcing terms proportional to $\sin(n\pi\tilde{t})\sin(n\pi s)$ and $\cos(n\pi\tilde{t})\sin(n\pi s)$ must be suppressed to prevent $O(\tilde{t})$ secular growth in u_2. As a result one obtains the secular equations for the Fourier coefficients α_k and β_k,

$$\left.\begin{aligned} \alpha_k' &= \tfrac{1}{16}(\gamma+1)\rho_0[4\alpha_k + k\pi(8\beta_0\beta_k + 2c_k - e_k)], \\ \beta_k' &= \tfrac{1}{16}(\gamma+1)\rho_0[4\beta_k + k\pi(-8\beta_0\alpha_k + 2d_k - f_k)], \end{aligned}\right\} \quad k = 1, 2, \ldots, \tag{90}$$

where

$$\left.\begin{aligned} c_k &= \sum_{n=1}^{\infty}(\alpha_n\alpha_{n+k} + \beta_n\beta_{n+k}), \\ d_k &= \sum_{n=1}^{\infty}(\alpha_n\beta_{n+k} - \alpha_{n+k}\beta_n), \end{aligned}\right\} \quad k = 1, 2, \ldots, \tag{91}$$

and

$$e_1 = 0, \quad f_1 = 0,$$

$$\left.\begin{aligned} e_k &= \sum_{n=1}^{k-1}(\alpha_n\alpha_{k-n} - \beta_n\beta_{k-n}), \\ f_k &= \sum_{n=1}^{k-1}(\alpha_{k-n}\beta_n + \alpha_n\beta_{k-n}), \end{aligned}\right\} \quad k = 2, 3, \ldots. \tag{92}$$

Equations (90)–(92) constitute an infinite system of nonlinear ordinary differential equations, in contrast to the linear secular equations (53) on the extended acoustic timescale, in which Fourier modes of different orders are decoupled from each other. The strong nonlinear mode coupling in c_k, d_k, e_k and f_k is the source of wave deformation and shock formation in the physical system, which will be demonstrated later. Note that the system of coupled equations in (90)–(92) is in general not solvable by analytical methods. Numerical solutions of the truncated, finite system can be obtained only when the function $\beta_0(\tau)$ is known *a priori*. We now develop the explicit form of $\beta_0(\tau)$ from the second-order velocity and density equations.

Once the resonant part of the forcing function is suppressed, (89) can be written as

$$u_{2\tilde{t}\tilde{t}} - u_{2ss} = \sum_{k=1}^{\infty}\sum_{n=1(n\neq k)}^{\infty}[\phi_{k,n}(\tau)\cos(n\pi\tilde{t}) + \psi_{k,n}(\tau)\sin(n\pi\tilde{t})]\sin(k\pi s), \tag{93}$$

where $\phi_{k,n}(\tau)$ and $\psi_{k,n}(\tau)$ are combinations of α_k, α_n, β_k and β_n, and are functions of τ only. Equation (93) should satisfy the homogeneous boundary conditions that can

be derived from (15) and (78). The general solution to (93) has a form similar to the forcing function on the right-hand side of the former equation,

$$u_2 = \sum_{k=1}^{\infty} \sum_{n=1}^{\infty} [\gamma_{k,n} \cos(n\pi\tilde{t}) + \delta_{k,n} \sin(n\pi\tilde{t})] \sin(k\pi s), \tag{94}$$

where $\gamma_{k,n}$ and $\delta_{k,n}$ are also functions of τ only, whose exact forms are irrelevant to the subsequent analysis. Equations (86), (87) and (94) can be used to rewrite (74) as

$$\rho_0^{\frac{1}{2}(\gamma+1)} \rho_{2\tilde{t}} = -\rho_0^{\frac{1}{2}(3-\gamma)} (\beta_0' - \tfrac{1}{2}(\gamma+1)\rho_0\beta_0) + \text{non-secular terms}. \tag{95}$$

One can suppress $O(\tilde{t})$ secular growth in ρ_2 if

$$\beta_0 = -\rho_0^{\frac{1}{2}(\gamma+1)}, \tag{96}$$

which satisfies the initial condition $\beta_0(\tau \to 0) = -1$.

Given $\beta_0(\tau)$ and initial conditions (84), the system of equations (90)–(92) can be truncated and solved numerically for $k = 1, 2, \ldots, N$. The infinite summations in c_k and d_k in (91) are approximated by summations from $n = 1$ to $n = N-k$ for this truncated system, to match the number of unknowns with that of the equations. The resulting $2N$ equations are solved simultaneously by employing the DVERK subroutine from the IMSL computer software library, which is based on the fifth- and sixth-order Runge–Kutta method designed by Hull, Enright & Jackson (1976). The step sizes of numerical integration are adjusted automatically in accordance with the specified relative error tolerance, which is set to be $\leqslant 10^{-6}$ for each time step. This error is sufficiently small in view of the larger truncation errors in approximating the originally infinite system. Since the truncation errors involved in approximating the infinite summations in (91) become significant when k gets close to N, only the first $\frac{1}{2}$ to $\frac{2}{3}$ of such computed coefficients are used to sum up the Fourier series. The results demonstrate that this truncated system can adequately describe the gasdynamic phenomena in the cylinder until shortly after the occurrence of the shock wave. Long after the shock formation, however, the convergence properties of the Fourier series become very poor because the accumulation of truncation errors eventually destabilizes the solution.

The total velocity and density of the gas can now be found by combining the results in this section,

$$u = \epsilon \left\{ (1-s) + \sum_{n=1}^{\infty} [\alpha_n(\tau) \cos(n\pi\tilde{t}) + \beta_n(\tau) \sin(n\pi\tilde{t})] \sin(n\pi s) \right\} + O(\epsilon^2), \tag{97}$$

$$\rho = \frac{1}{1-\tau} + \epsilon \left\{ -\frac{1}{(1-\tau)^2} + (1-\tau)^{-\frac{1}{2}(3-\gamma)} \times \sum_{n=1}^{\infty} [-\alpha_n(\tau) \sin(n\pi\tilde{t}) + \beta_n(\tau) \cos(n\pi\tilde{t})] \cos(n\pi s) \right\} + O(\epsilon^2). \tag{98}$$

The first term in (97) describes the time-independent bulk gas velocity correponding to spatially uniform compression by a constant-speed piston motion. The bulk density change is represented by the first two terms in (98), where the $O(\epsilon)$ correction is due to the non-constant velocity of the piston during the acceleration period. Superimposed on the bulk effects are acoustic phenomena described in terms of a Fourier representation. The amplitudes of the Fourier spatial modes in (97) and (98) are harmonic in time with growing frequency due to growing $\tilde{t}$, which is a generalization of the linear frequency growth exhibited in the extended acoustic time

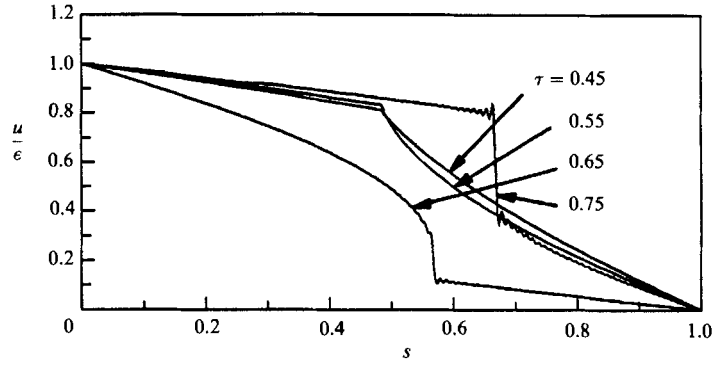

FIGURE 5. The velocity distribution in terms of the Lagrangian variable s during piston time compression as obtained from (97). The piston Mach number $\epsilon = 0.05$, and $\gamma = 1.4$.

solutions. Unlike the previous results in the last section (cf. (65), (66)) where the maximum value and the phase of the amplitude function for each Fourier mode are explicitly calculated as constants, they are now modulated by τ-dependent factors whose behaviour has to be determined numerically. This variation of the amplitude function on timescale τ causes the deformation of the acoustic disturbance. The amplitude of the fluctuating density is larger than that of the fluctuating velocity, and grows with piston time as a result of the multiplication factor in (98), which is related to the bulk compression effect.

The velocity distributions in the Lagrangian coordinate, like those in figure 3 for the extended acoustic timescale, are now depicted in figure 5 for specified piston times $\tau = 0.45$, 0.55, 0.65, and 0.75. The results are obtained by a summation of 200 Fourier terms in (97). Since the piston is moving at constant speed of 1 on this timescale, the velocity curves are bounded by 1 and 0 on both sides of the cylinder. The steepening of the acoustic wavefront with increasing τ eventually leads to shock formation. The steep portions of velocity curves at $\tau = 0.65$ and 0.75 in figure 5 are identified as shock waves based on the following reasoning:

When the Fourier series of a discontinuous function is plotted up to certain approximation, one obtains, instead of a real discontinuity, a sharp change of the function value over a narrow but finite region whose thickness is equal to half the wavelength of the highest-order spatial mode in the truncated series (Wang 1989). Near both sides of the region the solution exhibits oscillations known as Gibbs phenomena (Kármán & Biot 1940). By comparing the thickness of the steep portions in the velocity curves at $\tau = 0.65$ and 0.75 with the wavelength of the highest-order Fourier mode used in the summation, and by noticing the occurrence of the Gibbs phenomena, we conclude that the two seemingly non-vertical steep curves are virtually shock waves. A quantitative discussion about the slope of a Fourier-series-represented distributed 'discontinuity' has been given by Wang (1989).

The shock formation time in the cylinder, based on the above-mentioned method of shock identification, is found to be $\tau \approx 0.6$. It is observed that the shock first occurs at the very front of the continuously generated compression wave, increasing its strength with time as it propagates between the two solid boundaries. The situation is similar to unidirectional-propagating compression waves. The changing directions of wave propagation does not appear to alter the shock formation process fundamentally. When plotting figure 5 and the subsequent figures, we have computed α_1–α_{300} and β_1–β_{300} at 1600 time intervals from (90), and between 100–200

terms in the Fourier series are used. The computations were conducted on a CYBER 205. It is worth pointing out that we computed a large number of terms in the series in order to achieve sufficient resolution and steepness of the shock wave. One can obtain cruder but representative solutions with fewer Fourier modes (say, 50 terms) with a VAX-class mainframe computer without significant loss of accuracy, especially prior to shock formation.

6. Composite solutions

The preceding asymptotic results have been developed for both the short acoustic time regime and the more extended piston time period. For the purpose of compactness and convenience, it is desirable to derive a complete solution covering the whole time range of the piston-driven compression. Such uniformly valid composite expansions are formed by adding together solutions from different time regions and then subtracting from them the common parts (Kevorkian & Cole 1981). The composite solutions for velocity and density are constructed from (65), (66), (97) and (98) and take the form:

$$u = \epsilon\left\{(1-\mathrm{e}^{-t})(1-s)+\sum_{n=1}^{\infty}\left[\frac{2\mathrm{e}^{-t}}{n\pi(1+n^2\pi^2)} + \alpha_n(\tau)\cos(n\pi\tilde{t})+\beta_n(\tau)\sin(n\pi\tilde{t})\right]\sin(n\pi s)\right\}+O(\epsilon^2), \quad (99)$$

$$\rho = \frac{1}{1-\tau}+\epsilon\left\{\mathrm{e}^{-t}-\frac{1}{(1-\tau)^2}+\sum_{n=1}^{\infty}\left[\frac{2\mathrm{e}^{-t}}{1+n^2\pi^2} - (1-\tau)^{-\frac{1}{2}(3-\gamma)}(\alpha_n(\tau)\sin(n\pi\tilde{t})-\beta_n(\tau)\cos(n\pi\tilde{t}))\right]\cos(n\pi s)\right\}+O(\epsilon^2). \quad (100)$$

Once the small piston Mach number ϵ is specified, the dynamic response of the confined gas can be evaluated by using (99), (100) and the isentropic relations in (11) until $1-\tau \sim O(\epsilon)$, which marks the breakdown of expansion (100). Physically this corresponds to the time when the piston has almost reached the endwall of the cylinder.

Figure 6 displays the time variations of u at a set of specified Lagrangian coordinates for the case $\epsilon = 0.05$. Since each value of the Lagrangian coordinate represents a certain material point, these figures actually show the velocity at the indicated mass locations. In figures 6(*a*)–6(*d*) the magnified velocities u/ϵ at mass locations $s = 0, \frac{1}{4}, \frac{1}{2}$ and $\frac{3}{4}$, respectively, are plotted against the piston timescale τ. The smooth, slowly varying line in each figure describes the bulk velocity associated with spatially homogeneous compression. When the acoustic phenomena are added, the total velocity is observed to oscillate around the bulk value as a result of the repeated forward and backward transmissions of the compression wavefront. It is found that the velocity fluctuations are of the same order of magnitude as the bulk velocity, and that the maximum fluctuation occurs at $s = \frac{1}{2}$ (cf. figure 6*c*). In figure 6(*a*), $s = 0$ represents the impermeable piston face, whose velocity is given by the time derivative of the piston motion function (52), and on which no fluctuating velocity is allowed. The tooth-like shape of the velocity fluctuations in the u–τ plots can be explained from the results in figure 6(*d*). The piston-induced acoustic wavefront first reaches the given mass location at $\tau \approx 0.0375$ or $t \approx 0.75$. When the forward-running acoustic wavefront passes through the location, an increase in the particle velocity results. On the other hand, a backward-running acoustic wavefront tends to decrease the particle velocity. Repeated reflections of the compression wavefront give rise to

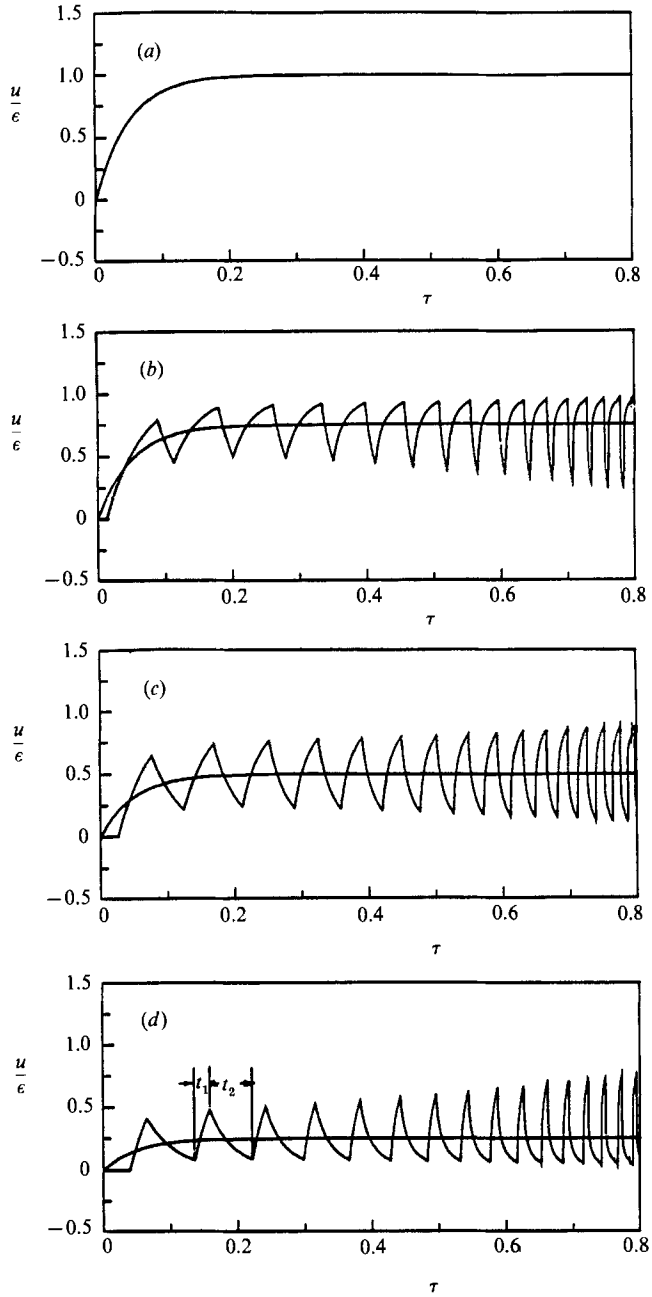

FIGURE 6. Velocity variations with piston time at specified material points s as obtained from (99). (*a*) $s = 0$, (*b*) $s = \frac{1}{4}$, (*c*) $s = \frac{1}{2}$, (*d*) $s = \frac{3}{4}$. The maximum piston Mach number $\epsilon = 0.05$, and $\gamma = 1.4$.

the alternating acceleration–deceleration process. The accelerating time t_1 corresponds to the round-trip time for the compression wavefront to travel between the given mass location and the cylinder endwall, while the decelerating time t_2 is the round-trip time between the mass location and the piston face. Except for the special case of $s = 0.5$, t_1 generally does not equal t_2 because of the asymmetrical locations of the two confining boundaries relative to the given material point. A comparison of figures

6(*b*), 6(*c*) and 6(*d*) shows that for increasing values of s the ratio t_1/t_2 decreases because the relative location of the material point is closer to the cylinder endwall. As time progresses the tooth-shapes in u–t plots are altered owing to the deformation of a sharp compression wavefront. At $\tau \approx 0.6$ line segments that are almost vertical begin to appear at corners of the teeth, where the fluid particles first encounter weak shocks formed at the wavefront. Because the shock has some finite thickness in the finite-sum approximation, the passage time of that finite zone is finite. Hence one should not expect absolutely vertical lines in the drawings. In fact the slope of the lines can be estimated from the shock 'thickness' and its speed. The length of the 'almost vertical' segments increases with increasing shock strength, as the nonlinear wave deformation processes continue. The calculations are terminated at $\tau = 0.8$ owing to limitations of the approximation method. The relatively large truncation errors cause unreliable results beyond this point. It is also noted that when $\tau = 0.8$ the asymptotic expansion (100) gets close to the point of breaking down.

Density variations with time are plotted in figures 7(*a*)–7(*d*), where each figure corresponds to the mass location and plotting conditions of its velocity counterpart in figures 6(*a*)–6(*d*). The upper curve ρ_b and lower curve ρ_a are extracted from equation (100) and represent the bulk compression term and the acoustic contribution, respectively. The former consists of terms outside the summation in (100), and the latter is the summation part in the equation magnified by a factor ϵ^{-1}. The total density is then $\rho = \rho_b + \epsilon\rho_a$. The bulk effects are spatially homogeneous and hence ρ_b curves are identical in figures 7(*a*)–7(*d*). The ρ_a curves in those figures are observed to be piecewise smooth. Each point of discontinuous derivative (and of discontinuous function itself after shock formation) between two smooth curve sections indicates the time when the compression wavefront arrives at the given material point. The portions of the ρ_a curve with the positive slope show the strong compression effect brought about by the wavefront. The portions with negative slope, on the other hand, show the weakening of the compression strength after the passage of the wavefront. The times t_1 and t_2 marked in figure 7(*d*) are the same round-trip times of the wavefront as those in figure 6(*d*), and their relative magnitudes depend on the relative mass location in the system. The two times are not equal in general, except when $s = \frac{1}{2}$ (cf. figure 7*c*). In figures 7(*b*) and 7(*d*) the smaller round-trip times correspond to the bumps on the wave-like ρ_a curves. In particular when $s = 0$, $t_1 =$ maximum and $t_2 = 0$. When the shock is formed in the gas medium, the positive-slope lines steepen up to form shock discontinuities, cutting the initially continuous curves into discontinuous pieces. If the total density ρ is plotted, it should consist of an initially undisturbed value, followed by a succession of oscillatory increases with time before shock formation, and stepwise increases after the shock formation. The maximum density fluctuation is found to exist at the two solid boundaries, i.e. the piston face and the cylinder endwall. Although density variations on the latter are not shown, it is worth pointing out that the ρ–τ curves at $s = 1$ have shapes similar to those in figure 7(*a*), except for a phase lag in the oscillatory acoustic modes.

In figure 6 the amplitude of the fluctuating velocity increases monotonically with time in such a way that the total velocity is always bounded by 0 and 1; the amplitude of the density fluctuations in figure 7, on the other hand, can be amplified without limit as the bulk density approaches infinity.

The increasing frequency of the compression wave passage with time in figures 6 and 7 is caused by two major effects. First, the acoustic velocity increases as the temperature rises from compressive heating and, secondly, the distance between the

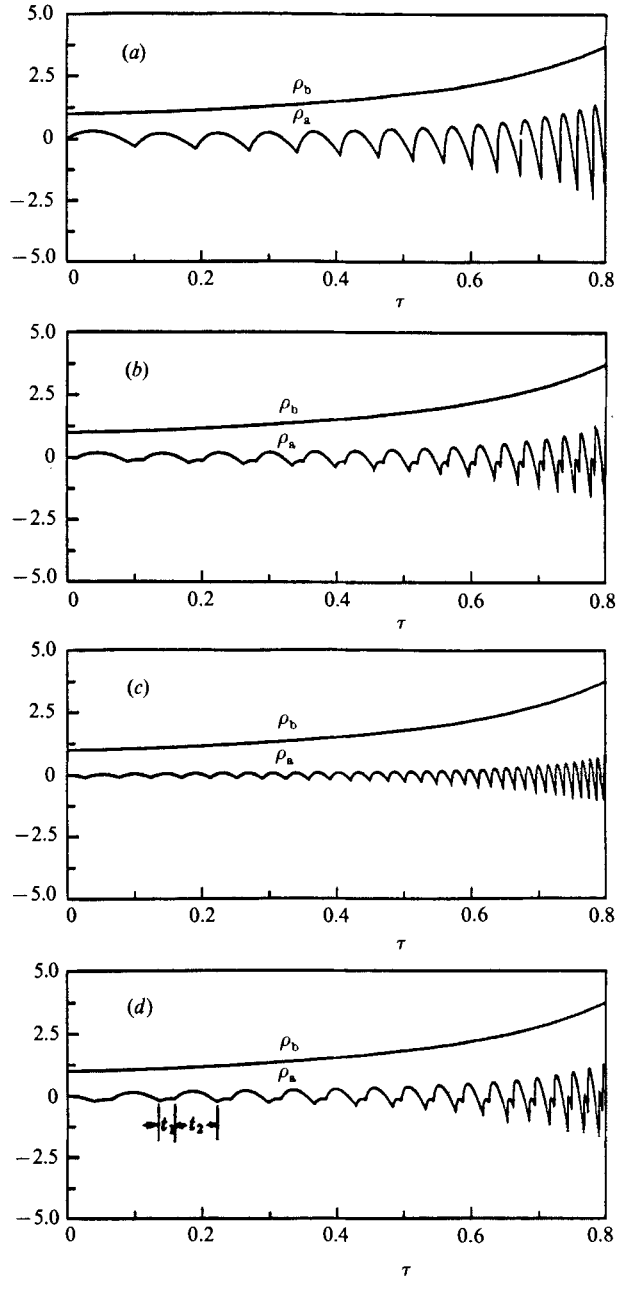

FIGURE 7. Density variations with piston time at specified material points s obtained from (100). ρ_b is the bulk density, and ρ_a is the density change due to acoustic contributions. The total density $\rho = \rho_b + \epsilon\rho_a$. (*a*) $s = 0$, (*b*) $s = \frac{1}{4}$, (*c*) $s = \frac{1}{2}$, (*d*) $s = \frac{3}{4}$. The maximum piston Mach number $\epsilon = 0.05$, and $\gamma = 1.4$.

piston and the top of the cylinder decreases with time. This frequency is also affected strongly by the piston Mach number. In figure 8 the density variation at the piston surface is given when $\epsilon = 0.1$, twice as much as the case plotted in figure 7. The faster piston speed allows for fewer acoustic wave reflections during one piston stroke. It is important to notice from figure 8 that the acoustic disturbance also steepens to

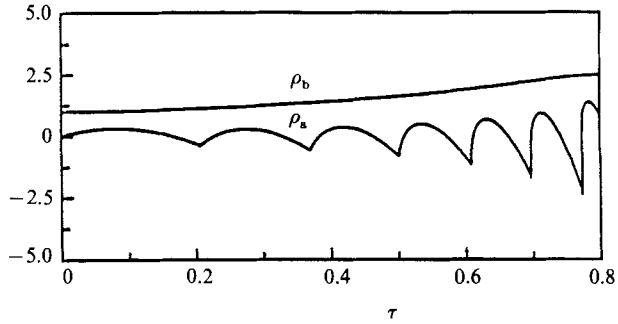

FIGURE 8. Density variations with piston time on the piston face $s = 0$ obtained from (100), for the case when the maximum piston Mach number $\epsilon = 0.1$, and $\gamma = 1.4$. ρ_b is the bulk density, and ρ_a is the density change due to acoustic contributions. The total density $\rho = \rho_b + \epsilon\rho_a$.

form a shock when $\tau \approx 0.6$, the same values as when $\epsilon = 0.05$. This shows that the shock formation time measured in terms of piston time units is invariant with the piston Mach number. In other words, the shock always occurs when the piston reaches a fixed position in the cylinder. This is because a compression wave of larger amplitude ($\sim\epsilon$ in the present case) will evolve into a shock within a shorter travelling distance and hence fewer reflections. From a mathematical point of view, this is clearly seen from secular equations (90)–(92) which are ϵ-independent, and which describe the development of nonlinear phenomena in the physical system.

7. Transformation to Eulerian coordinates

The inverse of the Lagrangian transformation in (13) can be combined with (100) to provide the $x = x(t, \tau, s)$ map,

$$x = s + (1-s)\tau + \epsilon\Big\{e^{-t} - 1 + (1-\rho_0^{-2}e^{-t})s - \rho_0^{-2}\sum_{n=1}^{\infty}\frac{1}{n\pi}\Big[\frac{2e^{-t}}{1+n^2\pi^2} - \rho_0^{\frac{1}{2}(3-\gamma)}(\alpha_n \sin(n\pi\tilde{t}) - \beta_n\cos(n\pi\tilde{t}))\Big]\sin(n\pi s)\Big\} + O(\epsilon^2). \quad (101)$$

In effect, this result provides the x-location of a material point s at a specified time τ given a specific value ϵ so that $t = \tau/\epsilon$ is known. When $\tau \to 0, x \sim s + O(\epsilon)$ where the $O(\epsilon)$ shift is due to events on the acoustic timescale t_a^*. Equation (101) is plotted in figure 9 for given specific material points. It shows that, except for the initially motionless period before the acoustic wavefront arrives at each location, the material points exhibit basically linear displacements with increasing time τ. The Fourier series summation in (101) is responsible for the small oscillations around the linear displacement process for $s = \frac{1}{4}, \frac{1}{2}$ and $\frac{3}{4}$, as is shown in figure 9. As τ increases, the amplitude of these oscillations decreases significantly. Note that although the velocity and density become discontinuous across the weak shock when it is formed, the displacement of material points remains always continuous because they all have finite speed.

By substituting (101) into (99) and (100), one can obtain the velocity and density distributions in Eulerian coordinates. Figure 10 shows the velocity and density history at the specified cylinder location $x = \frac{3}{4}$. The differences between figure 10 and figures 6(*d*) and 7(*d*) are to be noted. In the latter case Lagrangian coordinates are used. As time evolves, the distance between the location $x = \frac{3}{4}$ and the forward-

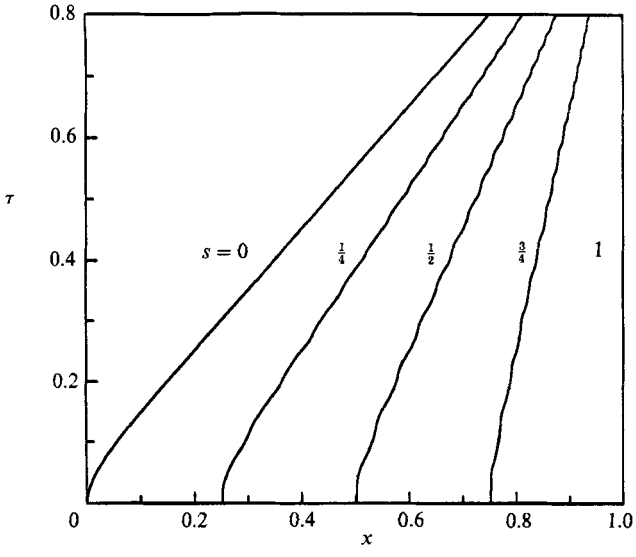

FIGURE 9. The displacement of material points $s = 0, \frac{1}{4}, \frac{1}{2}, \frac{3}{4}$ and 1 due to piston motion $X_p = \epsilon(t + e^{-t} - 1)$. The maximum piston Mach number $\epsilon = 0.05$, and $\gamma = 1.4$.

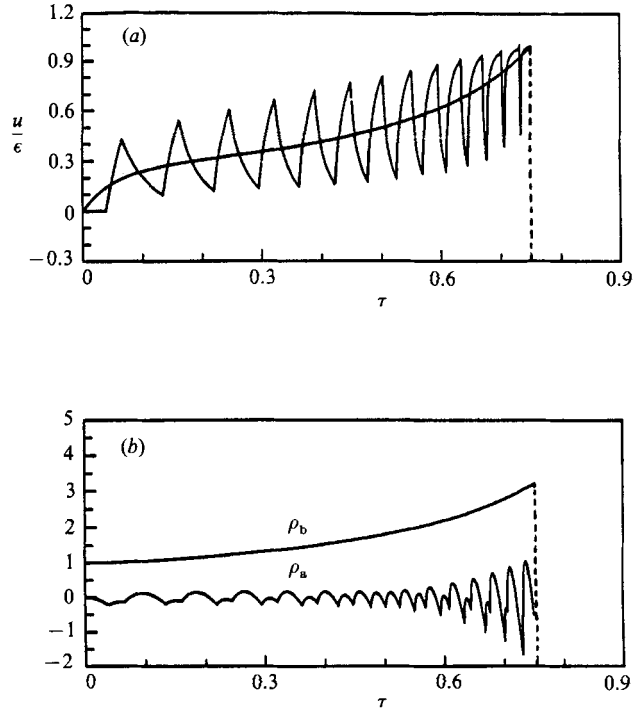

FIGURE 10. (*a*) Velocity and (*b*) density variations with piston time at spatial coordinate $x = \frac{3}{4}$. The maximum piston Mach number $\epsilon = 0.05$, and $\gamma = 1.4$.

moving piston decreases while that to the end of the cylinder remains constant. This shift of relative position causes changes in the relative magnitudes of the two previously mentioned round-trip times, t_1 and t_2, thus distorting the tooth-like u–τ and ρ_a–τ curves. The driving piston reaches $x = \frac{3}{4}$ when $\tau \approx 0.75$, at which time the

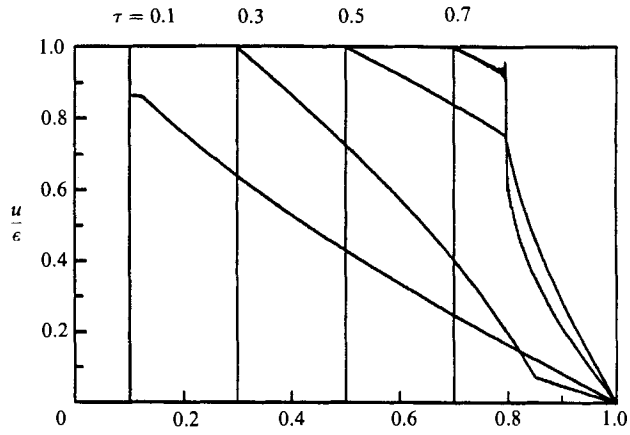

FIGURE 11. Spatial velocity distributions inside the cylinder on the piston timescale τ. The instantaneous piston position at each time value τ is indicated by a vertical line. The maximum piston Mach number $\epsilon = 0.05$, and $\gamma = 1.4$.

fluctuating velocity vanishes and the total velocity equals the piston speed. Meanwhile the density fluctuation reaches its maximum value. Again vertical portions of velocity and density curves appear at late stages, implying the formation of weak shock.

Velocity profiles inside the cylinder are plotted in figure 11, for four selected piston time instants covering almost the whole compression stroke. The instantaneous piston position corresponding to each time is indicated by a vertical line. The points with discontinuous x-derivatives on the velocity profiles for $\tau = 0.3$ and 0.5 are the instantaneous locations of the acoustic wavefront. When $\tau = 0.7$ a fully formed shock is present in which $\Delta u/\epsilon \approx 0.3$.

8. Conclusions

In the present paper the one-dimensional dynamic compression of an inert gas by a piston is considered. The gas is initially static. The piston Mach number increases smoothly from zero to a maximum value ϵ during a short acoustic time unit $t = O(1)$. On the more extended piston timescale $\tau = \epsilon t = O(1)$ the piston travels into the cylinder with a constant speed. The gasdynamic processes during the compression are modelled by the unsteady Euler equations. Asymptotic solutions are found in terms of single and multiple timescales in the limit of small piston Mach number. Solutions are constructed using a Fourier series technique to represent the evolving compression wave field of $O(\epsilon)$ generated by fast piston acceleration.

The solution approach developed in the present study is shown to be able to adequately describe the wave deformation and weak shock formation processes. The mathematical derivation is easier than that for the more traditional method of characteristics employed in the studies by Schneider (1981) and Klein and Peters (1988). Morever, it generates solutions that give explicit descriptions of the bulk motion and the instantaneous acoustic field, something difficult to extract from the characteristics calculations. A more comprehensive comparison between the two methods is discussed in a related paper (Wang & Kassoy 1990*b*).

Uniformly valid Fourier series solutions are obtained analytically for the linear acoustic field during the piston acceleration period, which is of the same order of magnitude as the acoustic timescale. The compression wavefront remains linear until

considerable piston displacement is attained. On the longer piston timescale during which significant compression of the gas occurs, the time-dependent coefficients in the Fourier series solutions are governed by an infinite system of coupled nonlinear ordinary differential equations. A numerical method is employed to find solutions to the truncated system to obtain the velocity and thermodynamic properties of the gas. The results show how nonlinear evolution on this timescale causes steepening of the compression wavefront. One observes the formation of a weak shock when the gas is compressed to approximately $\frac{2}{5}$ of its initial volume. The strength of the shock increases as it propagates back and forth between the two confining walls of the compressing system. Throughout the compression stroke repeated reflections of the acoustic or shock waves cause velocity and density fluctuations of the gas with time. The maximum velocity fluctuation appears in the middle plane between the moving piston face and the fixed cylinder endwall, while the maximum density fluctuation occurs at the two solid surfaces confining the gas. The accumulative effect of the wave passage is responsible for the spatially homogeneous bulk compression. As a result of the bulk compression, both the amplitude and frequency of the acoustic modes increase as the piston moves to fill the cylinder.

This research was supported by grants from the Mathematical Science Program of the Army Research Office DAAG29-85-K-0209 and DAAL03-88-K-0111. During the development of this work, fruitful discussions with, and enlightening suggestions from Professor Nobert Peters and Dr Rupert Klein of RWTH, Aachen, West Germany contributed substantially to the analysis and interpretation.

REFERENCES

Botz, R. E. & Tuve, G. L. 1973 *CRC Handbook of Tables for Applied Engineering Science*, 2nd edn. CRC Press.

Chester, W. 1964 Resonant oscillations in closed tubes. *J. Fluid Mech.* **18**, 44–64.

Courant, R. & Hilbert, D. 1953 *Methods of Mathematical Physics*, Vol. I. Interscience.

Evans, C. & Evans, F. 1956 Shock compression of a perfect gas. *J. Fluid Mech.* **1**, 399–408.

Hull, T. E., Enright, W. H. & Jackson, K. R. 1976 User's guide for DVERK – a subroutine for solving non-stiff ODEs. *TR* 100. Department of Computer Science, University of Toronto.

Kármán, T. von & Biot, M. A. 1940 *Mathematical Methods in Engineering*. McGraw-Hill.

Kassoy, D. R. 1979 The response of a confined gas to a thermal disturbance: slow transients. *SIAM J. Appl. Maths* **36**, 624–634.

Kevorkian, J. & Cole, J. D. 1981 *Perturbation Methods in Applied Mathematics*. Springer.

Klein, R. & Peters, N. 1988 Cumulative effects of weak pressure waves during the induction period of a thermal explosion in a closed cylinder. *J. Fluid Mech.* **187**, 197–230.

Landau, L. D. & Lifshitz, E. M. 1959 *Fluid Mechanics*. Pergamon.

Miles, J. W. 1971 *Integral Transformations in Applied Mathematics*. Cambridge University Press.

Obert, E. F. 1970 *Internal Combustion Engines*, 3rd edn. International Textbook Co.

Poland, J. & Kassoy, D. R. 1983 The induction period of a thermal explosion in a gas between infinite parallel plates. *Combust. Flame* **50**, 259–274.

Radhwan, A. M. & Kassoy, D. R. 1984 The response of a confined gas to a thermal disturbance: II Rapid boundary heating. *J. Engng Maths* **18**, 133–156.

Rott, N. 1980 Thermoacoustics. *Adv. Appl. Mech.* **20**, 135–174.

Schneider, G. H. 1981 Kompression und Expansion eines Gases in einem Zylinder als Störproblem. *Acta Mech.* **41**, 157–184.

Sirignano, W. A. & Crocco, L. 1964 A shock wave model of unstable rocket combustors. *AIAA J.* **2**, 1285–1296.

WANG, M. 1989 Piston generated dynamic compression and expansion of an inert gas in a cylinder. Ph.D Thesis, University of Colorado, Boulder.

WANG, M. & KASSOY, D. R. 1990*a* Dynamic response of an inert gas to slow piston acceleration. *J. Acoust. Soc. Am.* **87**, 1466–1471.

WANG, M. & KASSOY, D. R. 1990*b* Evolution of weakly nonlinear waves in a cylinder with a movable piston. *J. Fluid Mech.* **221**, 23–52.

ZEMANSKY, M. 1957 *Heat and Thermodynamics*, 4th edn. McGraw-Hill.